Bilirubin oxidase oriented on novel type three-dimensional biocathodes with reduced graphene aggregation for biocathode

Tang, Jing; Yan, Xiaomei; Huang, Wei; Engelbrekt, Christian; Duus, Jens Øllgaard; Ulstrup, Jens; Xiao, Xinxin; Zhang, Jingdong

Published in:
Biosensors and Bioelectronics

Link to article, DOI:
10.1016/j.bios.2020.112500

Publication date:
2020

Document Version
Peer reviewed version

Cite this paper: Jing Tang, Xiaomei Yan, Wei Huang, Christian Engelbrekt, Jens Øllgaard Duus, Jens Ulstrup, **Xinxin Xiao**, Jingdong Zhang; Bilirubin oxidase oriented on novel type three-dimensional biocathodes with reduced graphene aggregation for biocathode, ***Biosensors and Bioelectronics*** 2020, https://doi.org/10.1016/j.bios.2020.112500

Bilirubin oxidase oriented on novel type three-dimensional biocathodes with reduced graphene aggregation for biocathode

Jing Tang[a], Xiaomei Yan[a], Wei Huang[a], Christian Engelbrekt[a], Jens Øllgaard Duus[a], Jens Ulstrup[a,b], Xinxin Xiao[a,*], Jingdong Zhang[a,*]

[a] Department of Chemistry, Technical University of Denmark, Kongens Lyngby 2800, Denmark

[b] Kazan National Research Technological University, K. Marx Str., 68, 420015 Kazan, Republic of Tatarstan, Russian Federation

* Corresponding Authors: xixiao@kemi.dtu.dk (X. Xiao) and jz@kemi.dtu.dk (J. Zhang)

Abstract: Aggregation of reduced graphene oxide (RGO) due to π-π stacking is a recurrent problem in graphene-based electrochemistry, decreasing the effective working area and therefore the performance. Dispersing RGO on three-dimensional (3D) carbon paper electrode is one strategy towards overcoming this, which partially relieves aggregation. In this report, we describe the graft of negatively charged 4-aminobenzoic acid (4-ABA) onto a graphene functionalized carbon paper electrode surface. 4-ABA functionalization induces separation of the RGO layers, at the same time leading to favorable orientation of the blue multi-copper enzyme *Myrothecium verrucaria* bilirubin oxidase (*Mv*BOD) for direct electron transfer (DET) in the dioxygen reduction reaction (ORR) at neutral pH. Simultaneous electroreduction of graphene oxide to RGO and covalent attachment of 4-ABA are achieved by applying alternating cathodic and anodic electrochemical potential pulses, leading to a very high catalytic current density (Δj_{cat}:193 ± 4 μA cm^{-2}) under static conditions. Electrochemically grafted 4-ABA not only leads to a favorable orientation of BOD as validated by fitting a kinetic model to the electrocatalytic data, but also acts to alleviate RGO aggregation as disclosed by scanning electron microscopy, most likely due to the electrostatic repulsion between 4-ABA-grafted graphene layers. With a half-lifetime of 55 h, the bioelectrode also shows the highest operational stability for DET-type *Mv*BOD-based bioelectrodes reported to date. The bioelectrode was finally shown to work well as a biocathode of a membrane-less glucose/O_2 enzymatic biofuel cell with a maximum power density of 22 μW cm^{-2} and an open circuit voltage of 0.51 V.

Keywords: Reduced graphene oxide; bilirubin oxidase; carbon paper; 4-aminobenzoic acid monolayer; direct electron transfer; gas diffusion bioelectrode.

1. Introduction

Highly efficient and stable enzymatic bioelectrodes are key in the development of sustainable electrochemical bio-devices such as enzymatic biofuel cells (EBFCs), which presently attract increasing attention (Li et al., 2020; Ruff et al., 2018; Wang et al., 2020; Xiao et al., 2020; Xiao et al., 2019). The implementation of conductive nanomaterials for electrode modification offers here great promise (Le et al., 2016; Xiao et al., 2017; Xiao et al., 2019). Nanomaterials with high specific surface area improve enzyme loading, but are often accompanied by substrate diffusion limitations (Xiao et al., 2018; Zhao et al., 2017). Three-dimensional (3D) porous nanomaterials, with an open structure, simultaneously can alleviate limitations as to substrate supply and offer new possibilities for controlling enzyme orientation at the surface to facilitate direct electron transfer (DET) (Siepenkoetter et al., 2016; Xiao et al., 2018). In addition, 3D structures offer significant advantages through enzyme confinement, which ensures both efficient electronic coupling to the working electrodes (Siepenkoetter et al., 2017) and high enzyme stability (Mano and de Poulpiquet, 2018; Murata et al., 2009; Xiao et al., 2019).

Given its remarkable mechanical flexibility, favorable electronic properties, and light mass, graphene has recently been intensely studied as electrode support for bioelectrocatalysts for sensing or wearable bioelectronics applications (Pavlidis et al., 2014; Yu et al., 2019). However, pristine graphene itself, typically produced by mechanical exfoliation or chemical vapor deposition, has not been widely explored as bioelectrode material most likely due to the absence of functional surface groups such as carboxylic acid and amino groups suitable for enzyme immobilization (Wei et al., 2020). Reduced graphene oxide (RGO) is a better candidate for enzyme support due to the presence of residual oxygenated species on the basal planes and edges of the RGO sheets (Hernández-Cancel et al., 2015). RGO is usually produced chemically (Werchmeister et al., 2019), thermally (Dreyer et al., 2010) or electrochemically (Tang et al., 2019) based on an easy-to-handle

method. 3D graphene-based electrodes such as graphene papers (Shen et al., 2019a; Shen et al., 2019b) and graphene modified 3D electrodes (Tang et al., 2019; Werchmeister et al., 2019) with high surface area have emerged for enzymatic bioelectrodes with high catalytic current densities (Qiu et al., 2017). However, aggregation of RGO sheets is a recurrent problem, resulting in loss of active surface area (Dreyer et al., 2010). One strategy to relieve aggregation is to combine graphene with "spacers" such as carbon nanotubes (CNTs), polymers or silica particles (Lawal, 2019; Li et al., 2018; Yang et al., 2015). In our previous study (Tang et al., 2019), graphene oxide (GO) was reduced electrochemically directly onto 3D carbon paper (CPs), which resulted in well-performing bioelectrodes, but aggregation of RGO was not fully suppressed. Introducing hydrophilic surface groups such as sulfonic acid groups can also increase the dispersibility and separation of graphene layers in water (Zhao et al., 2011). Obtaining well-dispersed graphene free of aggregation while maintaining high electrical conductivity is thus paramount for bioelectrochemical applications.

Bilirubin oxidase (BOD) and laccase belong to the family of multi-copper oxidases (MCOs), and are known as efficient bioelectrocatalysts for the four-electron dioxygen reduction reaction (ORR) at mild pH (Gross et al., 2017; Xia et al., 2016a). MCOs have been widely immobilized on solid electrodes, serving as biocathodes for EBFC applications (Korani and Salimi, 2015; Mano and de Poulpiquet, 2018; Murata et al., 2009). MCOs hold four copper atoms, of three types: Cu_{T1}, Cu_{T2} and Cu_{T3} (Samejima et al., 1994). In ORR, Cu_{T1} receives electrons either from natural electron donors or from solid electrode surfaces (*i.e.* DET). The electrons are subsequently transferred to the trinuclear Cu_{T2}/Cu_{T3} center, where bound O_2 is reduced to H_2O (Al-Lolage et al., 2019; Gross et al., 2017). The electrocatalytic performance of well-oriented MCO on a solid electrode surface for dioxygen reduction is usually hampered by diffusion limitations and limited concentration of dissolved O_2 (~1.2 mM maximum at neutral pH and 1 atm O_2) in aqueous solution (Mano and de Poulpiquet, 2018). To circumvent this limitation, an air-breathing electrode, where O_2 would

85 diffuse directly from the air to the electrode, is practical (So et al., 2017). On the other hand, with
86 sufficient dioxygen supply, the rate of interfacial electron transfer between the electrode and the
87 Cu_{T1} site greatly affects the DET-electrocatalytic currents of MCO bioelectrode because the rate
88 decreases exponentially with increasing electron tunneling distance (Chi et al., 2005; Léger et al.,
89 2002; Mano and de Poulpiquet, 2018). Based on views on intramolecular electron transfer in
90 protein systems and quantum mechanical electron transfer concepts, efficient DET over more than
91 1.5 nm is not feasible (Chi et al., 2005; Gray and Winkler, 2010; Moser et al., 1992), highlighting
92 the importance of proper MCO orientation on the electrode for efficient electrocatalysis. Electrode
93 surface modification with substrate-mimicking molecules is an established approach to achieve
94 favorable MCO orientation on the electrode surface (Cracknell et al., 2011; Lopez et al., 2014;
95 Olejnik et al., 2012). The electrostatic and hydrophobic micro-environment around the Cu_{T1} site
96 is here crucial.
97 The most widely studied, *Myrothecium verrucaria* BOD (*Mv*BOD) undergoes efficient DET on
98 negatively charged surfaces (Lalaoui et al., 2015), while *Bacillus pumilus* BOD does so on
99 positively charged surfaces (Mazurenko et al., 2016). These studies highlight the importance of
100 understanding the specific enzyme at the molecular level and engineering of electrode surfaces at
101 the nanoscale. Another route is enzyme engineering introduced free cysteine residues which can
102 be specifically linked to electrode surfaces by covalent binding *via* maleimide groups (Al-Lolage
103 et al., 2019), enabling considerable DET of *Magnaporthae oryzae* BOD. Recently, high DET
104 bioelectrocatalytic current densities of BOD (up to ~0.2 mA cm^{-2} in static dioxygen-saturated
105 phosphate buffer solution, PBS) on electrochemically reduced GO electrodes modified with
106 negatively charged groups were achieved (Di Bari et al., 2016), but inevitable aggregation of the
107 ca. 200 μm GO flakes remained.

In order to overcome the problematic RGO aggregation, in the present study we have employed 3D CPs as supports for RGO modified with a negatively charged surface linker molecule 4-aminobenzoic acid (4-ABA) to enable highly efficient DET of *Mv*BOD. As a novel approach, the reduction of GO and grafting of 4-ABA were achieved simultaneously using electrochemical pulse treatment with cathodic and anodic potentials applied alternatively. Scanning electron microscopy (SEM) showed that RGO aggregation was in fact alleviated, implying that 4-ABA prevents π-π stacking of RGO due to electrostatic repulsion. 4-ABA also plays an important role in proper orientation of *Mv*BOD, validated both by high electrocatalytic current densities and by model simulation of the electrocatalytic currents. The BOD bioelectrode exhibits furthermore a surprisingly long half-life time of 55 h, to the best of our knowledge so far the best operational stability reported for *Mv*BOD. The bioelectrodes were then exploited in a gas diffusion electrode (GDE) configuration, registering elevated electrocatalytic current densities compared to the immersed bioelectrodes. The *Mv*BOD GDE was further used as a biocathode in a glucose/O_2 EBFC, demonstrating their potential to harvest electricity from sugars.

2. Experimental

2.1 Chemicals and materials

2,2'-Azino-bis(3-ethylbenzothiazoline-6-sulfonic acid) diammonium salt (ABTS, ≥98%), D-(+)-glucose (≥ 99%), potassium monohydrogen phosphate (K_2HPO_4, ≥ 99.999%) and potassium dihydrogen phosphate (KH_2PO_4, ≥ 99.999%) were from Fluka (Germany), potassium hexacyanoferrate(II) ($K_4[Fe(CN)_6]\cdot 3H_2O$, 99.0-102.0%) and potassium permanganate ($KMnO_4$, ≥99.9%) from Merck (Germany). Graphite powders (diameter < 20 μm), phosphorous pentoxide (P_2O_5, ≥ 98%), potassium peroxodisulfate ($K_2S_2O_8$, ≥ 99%), sulfuric acid (H_2SO_4, 95-97%), hydrogen peroxide (H_2O_2, 34.5-36.5%), hydrochloric acid (HCl, 37%), nitric acid (HNO_3, ≥ 65%), hexaammineruthenium(III) chloride ($[Ru(NH_3)_6]Cl_3$, 98%), N-cyclohexyl-N'-(2-morpholinoethyl)

carbodiimide methyl-p-toluenesulfonate (CMC, 95%) and 4-ABA (≥ 99%) from Sigma-Aldrich (USA). *Mv*BOD (lyophilized powder, 15-65 unit mg^{-1} protein, molecular mass 60 kDa) and glucose oxidase (GOD) (*Aspergillus niger*) (Type X+S. lyophilized powder, 100,000-250,000 units g^{-1} solid) were from Sigma-Aldrich (USA) and used as received. 190 μm-thick CP (product No. EC-TP1-060) was from Quintech (Germany), 210 μm-thick hydrophobic CP (HCP, product No. HCP120) and gas diffusion electrodes were from Shanghai Hesen Electric Co. Ltd (China). Glue guns (Product no. PKP 18 E) with hot melt adhesive (i.e. polyvinyl chloride) from BOSCH (Germany) were used to define a fixed geometric area of electrodes. 18.2 MΩ cm Millipore water was used throughout.

2.2 Fabrication of graphene-based bioelectrodes

The synthesis of GO using a modified Hummer's method is described in our previous reports (Seselj et al., 2018; Tang et al., 2019; Werchmeister et al., 2019). Prior to electrode modification, the working surface area (0.50 × 0.50 cm^2) of T-shaped CP was defined with hot melt adhesive using a glue gun, and coated with GO by sonication (denoted as CPG), Fig. S1 (Tang et al., 2019; Werchmeister et al., 2019). Based on the measured water contact angle (WCA), cf. below the resulting CPGs with different sonication duration were optimized to achieve surfaces of highest possible hydrophilicity, Fig. S2. We fabricated BOD bioelectrodes (RGO-A/BOD), Scheme 1, on the CPG substrates as follows: 20 μL GO suspension (3.0 mg mL^{-1}) was drop-cast onto a 0.25 cm^2 CPG electrode (labelled as CPG/GO electrode). After drying at room temperature (22 ± 2 °C), the CPG/GO electrode with a loading of 0.24 mg cm^{-2} GO was reduced and functionalized electrochemically by 15 cycles of alternating potential pulses at -1.4 V vs. Ag/AgCl (saturated KCl) for 10 s and 1.4 V for 5 s in 15 mL Ar-saturated PBS (100 mM, pH 7.0) containing 5 mM 4-ABA, resulting in the RGO-A electrode. The functionalized electrodes were washed with Millipore water to remove loosely adsorbed 4-ABA. The activation of the –COOH groups was

achieved by incubating the RGO-A electrode in 5 mM CMC aqueous solution for 2 h at 4 °C. Finally, 10 μL of 1.25 mg mL^{-1} BOD in 100 mM PBS (pH 7.0) was drop-cast onto the moist and activated RGO-A electrode. The RGO-A/BOD electrodes were dried for 12 h, and then stored at 4 °C in a high-humidity atmosphere, *i.e.*, a 5.5 cm plastic Petri dish containing a wet tissue. Control electrodes, including R-A/BOD without drop-cast GO suspension, RGO-A_ads/BOD where BOD was physically adsorbed by omitting the CMC activation step, and RGO/BOD in the absence of 4-ABA in PBS during electrochemical potential pulse treatment, were prepared similarly. Bioelectrodes with -1.4/0 V pulses (narrow pulse, RGO-A(N)/BOD), and 0/1.4 V (GO-A/BOD) where GO cannot be reduced, were prepared to investigate the role of potential pulse.

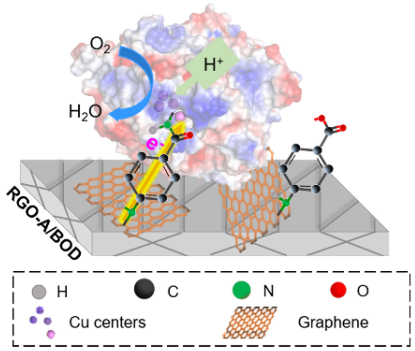

Scheme 1. Schematic illustration of the prepared RGO-A/BOD on a CPG electrode and its bioelectrocatalytic process. A possible orientation of *Mv*BOD, with surface charge distribution indicated by blue and red color symbolizing positive and negative charges, respectively, is shown (not drawn to scale). The electrostatic representation is qualitatively determined based on charge-smoothed potential from the PDB structure (2XXL) (Cracknell et al., 2011). The left 4-ABA linker forms an amide bond with BOD, while the right 4-ABA with free $–COO^-$ remains unreacted.

2.3 Characterization

The morphology of functionalized electrodes was characterized by SEM (Quanta FEG 200, FEI, USA) using an ETD detector. Atomic force microscopy (AFM) with a 5500 SPM system in tapping mode (Keysight Technologies, USA) was chosen to probe the functionalized graphene surface (*i.e.*, GO, RGO and RGO-A). X-ray photoelectron spectroscopy (XPS) of the modified electrodes was recorded using an X-ray photoelectron spectrometer (ESCALABMKII, Thermo

Scientific, USA). The surface hydrophilicity was characterized using a contact angle system (OCA Data Physics, Germany) to measure the WCA of dried electrodes with a droplet (6.0 μL) of Millipore water on top.

2.4 Electrochemical characterization

The basic electrochemical behavior of graphene modified electrodes without BOD was characterized by CV and electrochemical impedance spectroscopy (EIS) in 100 mM dioxygen-free PBS (pH 7.0) containing 5.0 mM $K_4[Fe(CN)_6]$ or $[Ru(NH)_6]Cl_3$ using an Autolab PGSTAT12 system (Eco Chemie, Netherlands) with the NOVA 2.1 software. A three-electrode setup was employed with graphene modified electrodes, a Pt wire, and Ag/AgCl (saturated) as the working, counter, and reference electrodes, respectively. EIS was conducted at 0.24 V vs. Ag/AgCl, with an applied amplitude of 10 mV in a frequency range 0.1 to 10^5 Hz. CV was recorded by scanning the potential from 0 to 0.65 V at a scan rate of 50 mV s^{-1}. CV in blank PBS at 5 mV s^{-1} was used to calculate the electrochemical surface area (ECSA).

CV, in the 0-0.65 V potential window at 5 mV s^{-1}, was used to characterize the ORR performance of the BOD bioelectrodes. Prior to electrochemical measurements, RGO-A/BOD bioelectrodes were immersed in 100 mM PBS (pH 7.0) for at least 30 min to remove loosely bound BOD molecules. 15 mL 100 mM pH 7.0 PBS bubbled with either Ar or O_2 for 30 min was used as blank electrolyte. The background-corrected ORR catalytic current density (Δj_{cat}), normalized to a geometric area of 0.25 cm^2, was obtained based on the difference between the cathodic currents at 0.2 V in Ar or O_2 saturated solution. The BOD bioelectrode operational stability was evaluated by chronoamperometry with an applied potential of 0.2 V in air-bubbled PBS (100 mM, pH 7.0).

2.5 Determination of amount of active BOD on the electrodes

The amount of active BOD immobilized on the electrodes was estimated from a standard calibration curve showing a linear relationship between the absorbance change of ABTS and the

amount of BOD in solution. In brief, the BOD bioelectrode was carefully washed five times with PBS (100 mM, pH 7.0) and then immersed into air-equilibrated 100 mM PBS (pH 7.0) containing 0.50 mg mL^{-1} ABTS with magnetic stirring. After soaking (i.e., 1, 3, 5, 7, 10 min), 500 μL of the reaction solution was withdrawn, and the absorbance measured at 420 nm with an ultraviolet - visible (UV-vis) spectrophotometer (UV-2401PC, SHIMADZU, Japan).(Durand et al., 2012)

2.6 Construction and characterization of gas diffusion bioelectrodes

The BOD bioelectrode was also exploited as a gas diffusion bioelectrode (GDBE) with accelerated gaseous substrate supply. A commercial HCP with one side treated with polytetrafluoroethylene (PTFE) which prevents electrolyte leakage, was used as the gas diffusion support for RGO-A/BOD. The detailed fabrication of the GDBE (surface area: 0.33 cm^2) is described in Supporting Information (SI). The electrochemical characterization was carried out using the three-electrode system in an in-house built electrolyte cell.

2.7 Applications of the GDE in membrane-less glucose/O_2 biofuel cells

A GOD bioanode was prepared according to our established procedure (Poon et al., 2018). Briefly, 39.2 μL solution, containing 3.3 mg mL^{-1} GOD, 2.0 mg mL^{-1} poly(ethylene glycol)diglycidyl ether (PEGDGE), and 3.2 mg mL^{-1} redox polymer $[Os(2,2'\text{-bipyridine})_2(polyvinylimidazole)_{10}Cl]^{+/2+}$ ($Os(bpy)_2PVI$), was drop-cast onto a nanoporous gold (NPG) electrode. After leaving the electrode in a vacuum desiccator for 20 min, the electrode was transferred into a refrigerator, allowing drying overnight at 4 °C. The GOD bioanode was assembled with the prepared GDBE biocathode and tested in the electrochemical cell containing 12 mL of PBS (100 mM, pH 7.0) with 20 mM glucose. No separating membrane was used due to the high selectivity of BOD and GOD. For the electrochemical characterization of glucose/O_2 EBFCs, the bioanode and biocathode were connected to the working and reference/counter electrode, respectively. LSVs with a scan rate of 1 mV s^{-1} were recorded to obtain polarization and power density profiles. The power density was

normalized to the cathode with a larger geometric surface area of 0.33 cm^2 compared to that of the bioanode.

3. Results and discussion

3.1 Characterization of electrode materials

CP consists of 3D-arranged carbon fibers and is suitable as the electrode substrate with high surface area (Chen et al., 2019). As suggested by SEM (Fig. 1a, S3a and S3b), GO is uniformly coated on the fibers. After electrochemical pulse potential treatment in the absence of 4-ABA, the GO nanomaterials coated on CP aggregate because the resulting RGO sheets tend to stack by π–π interactions (Fig. 1c and S3d). Notably, RGO-A shows the mildest aggregation compared to the RGO and RGO-A(N) (Fig. 1b and 1c, and S3c-f). This is most likely due to the presence of $–COO^-$ (in neutral solution) on the RGO sheets as introduced by the grafting of 4-ABA (Barbier et al., 1990; Yang et al., 2006). RGO-A with negative charges thus relieves π–π stacking due to electrostatic repulsion between the sheets.

For further investigation, GO, RGO and RGO-A were immobilized on highly oriented pyrolytic graphite (HOPG), described in SI, and characterized by AFM with good vertical resolution. It makes good sense that GO (1.2 ± 0.1 nm) is thicker than RGO (0.78 ± 0.03 nm) due to the removal of oxygenated groups *via* electroreduction, Fig. 1d, 1f, S4a-b, S5c-d, S5g-h and Table S1. RGO-A is ~5 Å thicker than RGO (Fig. 1e-f, S4b-c, S5e-f and Table S1), indicative of successful grafting of 4-ABA. Considering the distance (5.63 Å) between the N atom of the NH_2 group and the C atom of the COOH group of 4-ABA (Fig. S6) as well as the projected lengths of the C-O and N-H bonds plus van der Waals and hydration lengths, the estimated length of 4-ABA is larger and might be up to 6-7 Å suggesting that the grafted 4-ABA is tilted on the RGO surface.

XPS was chosen to map the surface chemical compositions and carbon bonding states of the modified electrodes. The percentages of each carbon species relative to the total amount of carbon

252 species, based on the relative surface area of each fitted peak, Fig. 1g-i and S7a-c, with the
253 corresponding binding energies are summarized in Table S2 (Seselj et al., 2018; Tang et al., 2019).
254 The trend of relative surface area of oxygenated carbon species for the electrodes is consistent with
255 the O/C ratio in the survey spectra, indicating satisfactory fitting, Table S2 and Fig. S7d. As noted,
256 the relative amount of oxygenated carbon species including C–O, C=O and COO– increases
257 drastically from 2.3% and 36.7% to 54.8% for bare carbon paper (CP), CP coated with GO (CPG),
258 and CPG with drop-cast GO (CPG/GO), respectively. This variation is caused by the presence of
259 GO with substantial amounts of oxygenated carbon species on the CPG and the increasing amount
260 of immobilized GO on the CPG/GO electrodes.(Tang et al., 2019). After electrochemical potential
261 pulse treatment, the total amount of oxygenated species on the CPG/GO electrodes decreases
262 notably to 18.0%, 14.5% and 8.6% for the RGO, RGO-A and RGO-A(N) electrodes, respectively.
263 This is reasonable because the precursor electrode (*i.e.* CPG/GO) is likely to be electrochemically
264 reduced when a negative potential pulse of -1.4 V is applied, meaning that the GO on the electrode
265 is converted to RGO with much fewer oxygenated groups (Tang et al., 2019). Compared to the
266 RGO electrode with the inevitable C-N impurities (4.4%), larger amounts of C–N species on RGO-
267 A (16.3%) electrodes reflect the successful modification of 4-ABA undergoing electrochemical
268 oxidation at 1.4 V. A small amount of C–N species (5.0%) on RGO-A(N) after the potential pulse
269 of -1.4/0 V due to the presence of physically adsorbed 4-ABA can also be determined. In summary,
270 the observations demonstrate that the electrochemical -1.4/1.4 V potential pulsing can achieve both
271 electroreduction of GO and electro-oxidation of 4-ABA on the CPG/GO electrode in a single step.

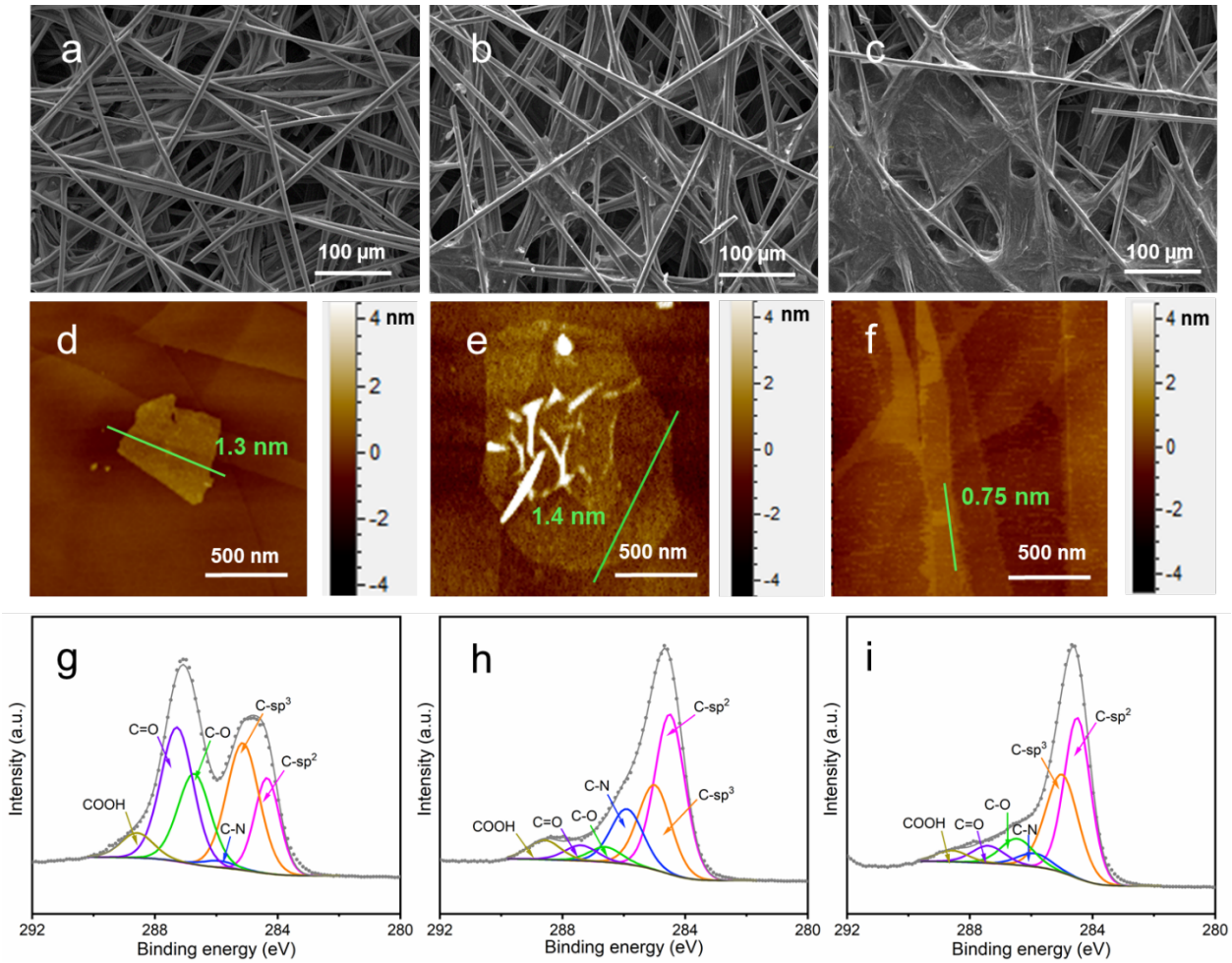

Fig. 1. SEM, AFM images and XPS spectra of (a, d and g) GO, (b, e, and h) RGO-A and (c, f and i) RGO nanomaterials. CP is the substrate for SEM and XPS, while flat HOPG is the support for AFM. The cross-section profiles are shown as Fig. S4.

3.2 Electrochemical characterization of the modified electrodes

Prior to enzyme immobilization, various CP based electrodes were characterized by. EIS in 100 mM PBS (pH 7.0) containing 5.0 mM $K_4[Fe(CN)_6]$ was first carried out. The impedance spectra were fitted using the equivalent circuit in Fig. 2a (Tang et al., 2019). The primary electrode (CPG/GO) gives a moderate charge transfer resistance (R_{ct}) of 50.6 Ω, Table S3. GO-A shows the highest R_{ct} of 341 Ω, in good agreement with the largest peak separation (ΔE_p) of 286 mV and the smallest anodic peak current (0.50 mA cm^{-2}) for the CV of $[Fe(CN)_6]^{3-/4-}$, Fig. 2b and Table S4. The significantly increased R_{ct} and ΔE_p are mainly caused by the stronger electrostatic repulsion

between the redox probe $[Fe(CN)_6]^{3-/4-}$ and the increased amount of –COOH groups (mostly in –COO^- form at pH 7.0), on the surfaces after electrochemical oxidation of 4-ABA. This is supported by the significantly smaller ΔE_p for positively charged $[Ru(NH_3)_6]^{2+/3+}$. On the other hand, negative potential pulses can reduce GO on the electrode surface and improve the electrode conductivity, supported by R_{ct} decreasing from 50.6 Ω for CPG/GO to 29.0 Ω for the resulting RGO, together with a smaller ΔE_p (from 146 to 105 mV, and from 166 to 107 mV) for both $[Fe(CN)_6]^{3-/4-}$ and $[Ru(NH_3)_6]^{2+/3+}$. When CPG/GO was treated electrochemically with both negative and positive potential pulses, the resulting RGO-A electrode similarly shows a smaller R_{ct} of 32.6 Ω compared to the CPG/GO electrode, consistent with CVs with smaller ΔE_p of 112 and 142 mV for $[Fe(CN)_6]^{3-/4-}$ and $[Ru(NH_3)_6]^{2+/3+}$, respectively. In addition, R_{ct} and ΔE_p for $[Fe(CN)_6]^{3-/4-}$ of RGO-A are comparable to those of RGO and RGO-A(N). This is reasonable, as electroreduction of GO greatly enhances the electrochemical activity. Notably, RGO-A(N) shows the smallest ΔE_p (105 mV) for $[Ru(NH_3)_6]^{2+/3+}$ probably due to physically adsorbed 4-ABA efficiently attracting the positively charged redox probe molecules.

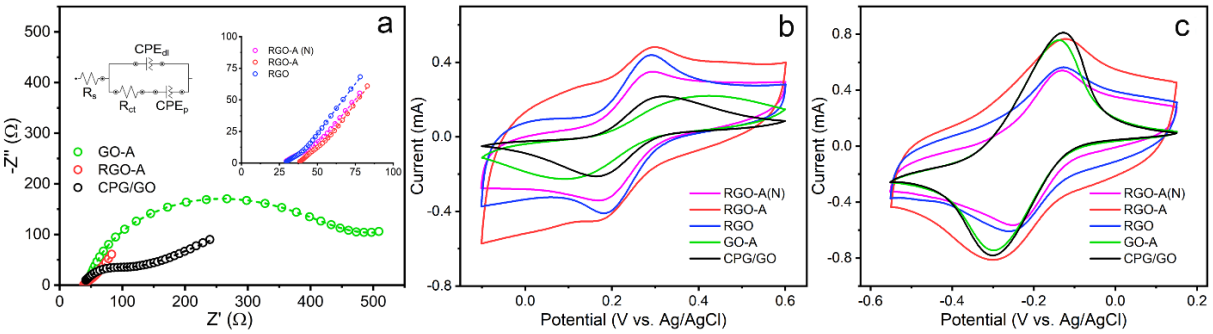

Fig. 2. (a) EIS of CPG/GO, RGO-A and GO-A electrodes in 100 mM O_2-free PBS (pH 7.0) with 5.0 mM $K_4[Fe(CN)_6]$. Inset right in (a): Magnified EIS of RGO-A compared with RGO-A(N) and RGO electrodes. Inset left in (a): Equivalent circuit used for fitting the impedance data. R_s: electrolyte solution resistance. R_{ct}: interfacial electron transfer resistance. CPE_{dl} and CPE_p: constant phase element of the electrode double layer and polarization, respectively. CVs at 50 mV s^{-1} of CPG/GO, GO-A, RGO, RGO-A and RGO-A(N) electrodes in 100 mM O_2-free PBS (pH 7.0) with 5.0 mM (b) $K_4[Fe(CN)_6]$ or (c) $[Ru(NH)_6]Cl_3$.

ECSAs of the modified carbon electrodes were estimated roughly from the capacitive currents based on CVs in PBS electrolyte for internal comparison (Tang et al., 2019; Wernert et al., 2018) ,

Fig. S8 and Table S5. This method is widely used in electrochemistry, since the capacitive current mainly depends on the surface area of the electrode although it could be affected by deviation of the specific capacitance for the modified electrode (Trasatti and Petrii, 1991). Bare CP shows the smallest ECSA of 0.010 ± 0.001 cm^2. CPG shows 50-fold increased ECSA, and CPG/GO nearly further doubles the ECSA of CPG to 1.0 ± 0.2 cm^2 because of the improved hydrophilicity, Fig. S2. Electroreduction of GO to RGO results in a RGO electrode with an ECSA notably increased to 45 ± 8 cm^2 due to the improved conductivity. The RGO-A electrode exhibits the largest ECSA (82 ± 10 cm^2) among the reduced electrodes RGO (45 ± 8 cm^2) and RGO-A(N) (42 ± 4 cm^2), consistent with the SEM observation that the RGO-A electrode shows the mildest RGO sheet aggregation. Overall, the RGO-A electrode with the relatively low R_{ct} and the highest ECSA could be an excellent matrix for BOD immobilization. Both morphology and electrochemical studies thus show that 4-ABA grafting alleviates RGO aggregation by electrostatic repulsion and thus attenuates π–π stacking. After enzyme immobilization, similar trends have been observed, but all ESCAs decrease by about 50% probably due to the presence of insulating protein (Table S5). Overall BOD immobilization and electrocatalytic characterization are therefore accommodated on a set of novel type electrodes which are very well characterized.

3.3 Electrocatalysis of BOD bioelectrodes

The ORR on the RGO-A bioelectrodes with BOD immobilized was found to set in at approximately 0.57 V vs. Ag/AgCl (Fig. 3a), consistent with reported observations for other electrode systems (Gutierrez-Sanchez et al., 2016; Xia et al., 2016a). RGO-A/BOD (193 ± 4 μA cm^{-2}) shows 3.4-fold higher Δj_{cat} compared to R-A/BOD (44 ± 5 μA cm^{-2}), Fig. 3a. This can be explained by the more facile electron transfer through the electrode due to the higher RGO content on RGO-A/BOD over R-A/BOD, as disclosed by the increased estimated ECSA from 10 ± 1 cm^2 for R-A/BOD to 48 ± 3 cm^2 for RGO-A/BOD (Fig. 3a and Table S5). The loading value of RGO

materials governs the "effective" surface area and surface addressability of the modified electrodes. This could be further verified by tuning the amount of drop-cast GO (*i.e.* the amount of resulting RGO) from 1.0 to 3.0 mg mL^{-1} correspondingly reflected in Δj_{cat} of the BOD bioelectrodes, Fig. 3b. It is seen that ECSA and Δj_{cat} both increase with increasing concentration of drop-cast GO, until a maximum is reached at 3 mg mL^{-1}. Further increasing concentration of GO solution for electrode modification leads to decreasing Δj_{cat} in spite of a further increased ECSA, Fig. 3b. The decreased catalytic response is probably due to blocked CP network posing diffusion limitation of the substrate O_2 from bulk solution to the electrode surface. This is supported by SEM, which shows that macropores of CP are blocked by highly concentrated RGO aggregation (Fig. S3g). It was, however, clearly confirmed that the dispersed RGO modified 3D bioelectrodes even with lower ECSA showed superior substrate diffusion and catalytic performance than the aggregated RGO modified bioelectrodes.

The RGO-A bioelectrode shows a 1.4-fold higher catalytic response compared to the RGO bioelectrode, Fig. 3c, highlighting the role of 4-ABA as a DET promotor grafted on the electrode surface by applying the positive potential pulse (Fig. S9 and S10a). This step is essential for favorable orientation of BOD, since the Cu_{T1} site of *Mv*BOD, surrounded mainly by positive charges at neutral pH (Scheme 1), is then close to the RGO-A electrode surface (Chen et al., 2019). In addition, the RGO-A bioelectrode shows a 2.9-fold higher catalytic response compared to the aggregated RGO-A(N) matrix obtained without positive potential pulse, *i.e.* no chemical grafting of 4-ABA, Fig. S10b. The presence of physically adsorbed 4-ABA on the RGO-A(N) matrix, concluded from XPS (Table S2), could thus still orient BOD to an extent. However, in comparison to RGO-A, RGO-A(N) suffers more serious RGO aggregation, blocking the micropores of 3D CP, and resulting in poorer orientation of BOD for DET as well as slow substrate O_2 diffusion compared with RGO-A. Only 2.6% catalytic activity on the GO-A/BOD bioelectrode compared

to RGO-A/BOD, Fig. S10b was observed, highlighting further the importance of electroreduction for improved electrode conductivity. This is supported by the observation that the GO-A/BOD electrode shows only 4.4% ECSA of the RGO-A/BOD electrode, Table S5. Compared to reported BOD behavior on aggregated RGO (size: ca. 200 µm) carbon electrodes with linkers similar to 4-ABA, our RGO-A/BOD bioelectrode showed comparable catalytic performance, but with much smaller amounts of drop-cast enzyme (12.5 vs. 80 µg (Di Bari et al., 2016)). This reflects the superiority of our dispersed RGO-A over aggregated RGO and therefore the very favorable BOD orientation in our RGO-A modified 3D structured electrode in DET-type bioelectrochemistry. It is worth mentioning that the maximum catalytic current density (Δj_{cat}:193 ± 4 µA cm^{-2}) of our optimized bioelectrodes is obtained in O_2-saturated electrolytes under static conditions, while most reported catalytic responses were obtained from rotating electrodes. The catalytic response obtained in our study is limited by the O_2 diffusion from the bulk solution to the electrode surface. We have prepared a summary table in which the electrocatalytic performance (Δj) of DET-type *Mv*BOD for ORR under static conditions (Table S6) on different surface matrices are compared. Our bioelectrode is seen to show the best competitive performance using the smallest amount of BOD. Different from previous biocathodes as shown in Table S6, CPG/RGO-A is fabricated *via* a facile electrochemical treatment of CPG with RGO and subsequent immobilization of *Mv*BOD. Additionally, CPG/RGO-A can be easily adopted for gas-diffusion electrodes as discussed in Section 3.6.

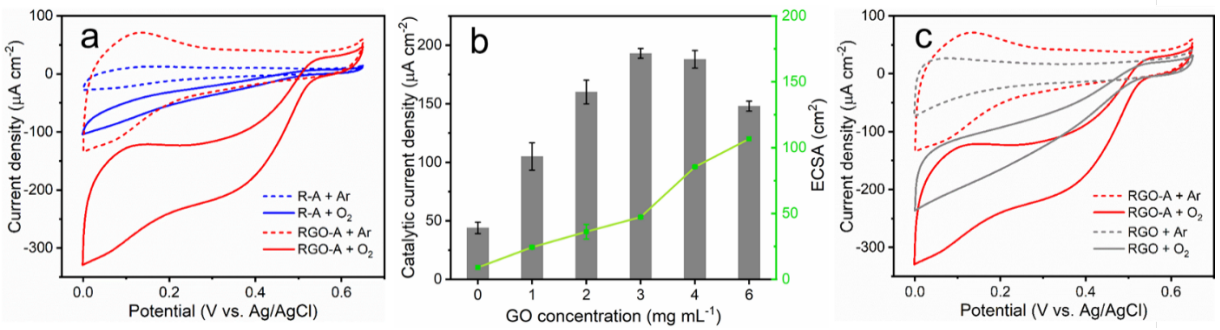

Fig. 3. CVs of the BOD bioelectrodes based on (a) R-A and RGO-A matrices, as well as (c) RGO-A and RGO matrices in 100 mM PBS (pH 7.0), scan rate 5 mV s^{-1}. (b) Effect of the amount of drop-cast GO (20 µL) on the electrocatalytic performance toward O_2 reduction as well as ECSA of RGO-A/BOD electrodes. All catalytic currents are collected at 0.2 V and background-corrected.

3.4 Kinetic analysis of the bioelectrode performance

We undertook a more detailed kinetic analysis to achieve a better understanding on how 4-ABA functionalization promotes the DET of BOD. The amount of active BOD immobilized on the electrode could, first be estimated by enzyme assay using a spectroscopic method, Fig. S11. The estimated surface coverage, Γ_{act}, of all active BOD in the RGO-A matrix (64 ± 3 pmol cm^{-2}) is comparable to the coverage on the RGO (58.0 ± 0.7 pmol cm^{-2}) and RGO-A(N) matrices (49.3 ± 0.7 pmol cm^{-2}), although Δj_{cat} on these three electrode matrices varies somewhat, Table S7. The highest Δj_{cat} on RGO-A is therefore mainly due to higher ratio of BOD able of DET as a result of better enzyme orientation, rather than higher enzyme loading. Further, the catalytic rate constant of immobilized BOD, k_{cat}, is estimated based on the experimental linear sweep voltammetric data for the catalytic current (i) vs. the electrode potential E.

Further, to illuminate further the BOD surface binding in the presence and absence of 4-ABA, we treated the data using the model of dispersive catalytic interfacial electron transfer rate constants introduced by Armstrong and associates (Léger et al., 2002) and recently exploited also by Kano and associates (Takahashi et al., 2019; Xia et al., 2016a). Dispersion is incorporated in this model by a uniform distribution of electron transfer distances (d) within a certain range between d_{min} and $d_{min}+\Delta d$, over which electrochemical electron transfer between the electrode and the Cu_{T1} center can occur. Within this range, the standard electrochemical electron transfer rate constant, k_0 is assumed to follow the tunneling form:

$$k_0 = k_0^{max} exp[-\beta(d_{min} + \Delta d)] \quad (1)$$

β is the decay factor for tunneling through the intermediate "matter" between the electrode and the Cu_{TI} center (≈ 1-1.4 Å^{-1}). k_0^{max} is a standard rate constant at the lower limit of the distance or orientation distribution ($d = d_{min}$), over which interfacial ET through the protein is feasible. With the presence of the 4-ABA layer, residual tunneling may be inherent also in k_0^{max}.

In the model by Armstrong and associates the catalytic current, i is recast as the i/i_{lim}^{cat} vs. E in the two-step form (Léger et al., 2002; Takahashi et al., 2019; Xia et al., 2016a).

$$\frac{i}{i_{cat}^{lim}} = \frac{1}{\beta\Delta d\{1+exp(\varphi)\}} \ln\left|\frac{\{1+\exp(\varphi)\}+\frac{k_{cat}}{k_0^{max}}exp(\alpha\varphi)}{exp(-\beta\Delta d)\,\{1+exp(\varphi)\}+\frac{k_{cat}}{k_0^{max}}exp(\alpha\varphi)}\right| \quad (2)$$

$$\varphi = \frac{n_E' F}{RT}(E - E_E^{0\prime}) \quad (3)$$

$i_{cat}^{lim} = (n_S/n_E)\, F \times k_{cat}\lambda\Gamma_{act} \times A$ is the limiting, enzyme controlled current density, where n_S is the number of electrons for the reduction of substrate dioxygen (4), n_E the number of electrons transferred in the enzyme (1), and A the geometric electrode surface area (0.25 cm^2). A (potential independent) enzyme "surface orientation factor", λ (< 1), represents the fraction of the total amount of adsorbed active enzyme capable of DET, so $\Gamma_{DET} = \lambda\Gamma_{act}$. α is the transfer coefficient (0.5), n_E' the number of electrons for interfacial electron transfer between Cu_{T1} and the electrode (1), F the Faraday constant (96485 s A mol^{-1}), R the gas constant (8.314 J·K^{-1}·mol^{-1}), T the absolute temperature (293 K), and $E_E^{0\prime}$ the formal redox potential of the Cu_{T1} site of BOD that communicates with the electrode by DET (0.473 V vs. Ag/AgCl) (Christenson et al., 2006; Mano and de Poulpiquet, 2018). It is noted that the second step is viewed as a direct single-step intramolecular communication step between the Cu_{TI} center and the substrate reduction at the catalytic Cu_{T2}/Cu_{T3} site.

Following previous reports (Takahashi et al., 2019; Xia et al., 2016a), k_{cat}/k_0^{max}, $\beta\Delta d$, and $k_{cat}\lambda\Gamma_{act}$ were used as adjustable parameters to fit Eq. (2) and (3) to the recorded LSV data, Fig. 4a.

The catalytic rate constant for DET-capable enzymes, k_{cat}, is different from the solution activity (k_c) due to the different nature of the electron donors. In order to get reasonable fitting, k_{cat}/k_0^{max} is considered as fixed for all the different electrodes. The center of catalytic activity of BOD is thus somewhat remote from the surface and k_{cat} therefore not likely to vary greatly on similar RGO-based electrodes. We shall also take k_0^{max} to be the same for all the ABA-modified electrodes since k_0^{max} largely involves electron transfer (tunneling) across the interface from the carbon surfaces through the bound ABA-unit as well as reorganization free energy terms and other rate parameters that vary little on the protein side. In view of the small structural extension of the bound ABA, tunneling through ABA is only weakly attenuated and may even belong to the adiabatic limit of strong interaction with the electrode surface. With these reservations, the same value of $k_0^{\max}$ may be taken also for the electrodes with no bound A. The estimated $k_{cat}\lambda\Gamma_{act}$ for the RGO-A matrix (373 ± 2 pmol cm^{-2} s^{-1}) is higher than for RGO (320 ± 40 pmol cm^{-2} s^{-1}) and RGO-A(N) (156 ± 1 pmol cm^{-2} s^{-1}), in accordance with the trend of Δj_{cat} on these three electrode matrices, Table S7. Furthermore, considering the values for Γ_{act} on the corresponding matrices obtained by the activity assay, and still taking the catalytic activities (k_{cat}) as similar, a larger orientation parameter λ for RGO-A compared to RGO-A(N) is proposed as a main contributor to the improved catalytic performance. However, a comparable λ obtained on RGO-A and RGO would indicate that there is another contributor.

$\beta\Delta d$ is evaluated to be smaller than 1 for the RGO-A/BOD electrode, but larger than 8 for the RGO/BOD and 5.0 ± 0.1 for RGO-A(N)/BOD electrodes, Table S7. If β is taken to be 1.0-1.4 Å^{-1} for all the electrodes (Moser et al., 1992), then Δd is formally less than 0.7-1.0 Å for RGO-A/BOD, and in the ranges of 5.7-8.0 Å^{-1} and 3.5-5.1 Å^{-1} for RGO/BOD and RGO-A(N)/BOD, respectively. Δd for RGO-A/BOD is also smaller than the reported value (2.6 ± 0.2 Å) for BOD on a planar electrode (Xia et al., 2016a), indicative of more favorable and narrower BOD orientation

distribution on RGO-A electrodes than on all the other electrodes. Taking into account that the BOD size is 4-6 nm (Xia et al., 2016a), most of the DET-capable BOD on the RGO-A matrix would then be in quite narrow orientation distributions. The favorable BOD orientation on the RGO-A matrix is due to the abundance of negatively charged aromatic groups. Based on these kinetic analyses, the promoted DET-type biocatalysis on the RGO-A matrix is thus concluded to be due to the most favorable orientation of BOD (the smallest Δd and largest λ) promoted by the aromatic 4-ABA groups on the electrode surface**.**

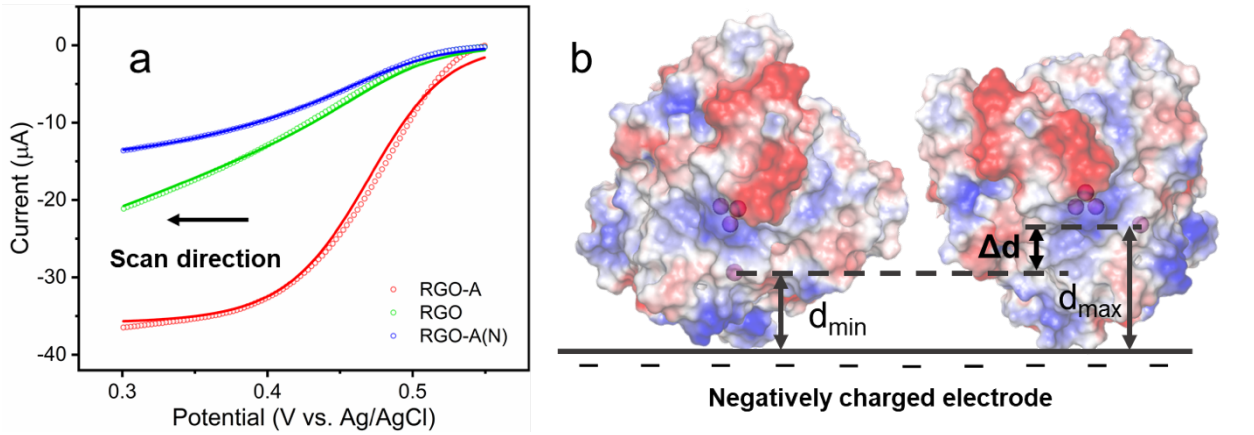

Fig. 4. (a) Linear sweep voltammograms of catalytic reduction of dioxygen for BOD on RGO-A, RGO or RGO-A(N) matrices at a scan rate of 1 mV s^{-1} in dioxygen-saturated PBS (pH 7.0). The dotted and solid lines represent the raw voltammogram and fitted curves, respectively. (b) Schematic illustration of two boundary orientations of BOD on a negatively charged electrode surface, resulting in different tunneling distances *d* for interfacial electron transfer from the electrode to the BOD Cu_{T1} site.

3.5 Stability of bioelectrodes

We investigated further the storage and operational stability of the BOD bioelectrodes. The RGO-A bioelectrode shows the best storage and operational stability compared to control bioelectrodes, i.e. the RGO bioelectrode and the RGO bioelectrodes with adsorbed 4-ABA (RGO-A(N)), Fig. 5 and S12. For example, after two-week storage, the RGO-A bioelectrodes retain 50% of initial catalytic response while the RGO and RGO-A(N) bioelectrodes only retain 25% of the initial value. This highlights the role of 4-ABA in maintaining the electrode stability. Similar to reported

polycyclic aromatic electrode surface modifiers such as phenylalanine, tyrosine and tryptophan (Blanford et al., 2009), grafted 4-ABA binding to the Cu_{T1} site pocket of the enzyme is proposed further both to stabilize BOD binding and to attenuate conformational changes and therefore denaturation of bound BOD (Gutierrez-Sanchez et al., 2016). Although freshly prepared RGO-A_ads/BOD bioelectrodes, in which BOD is physically adsorbed on the electrode, show a comparable initial electrocatalytic activity and similar kinetic parameters as covalently bound BOD on RGO-A, Table S7, only 35% of the original Δj_{cat} is retained after two weeks' storage. This can be ascribed to BOD leaching from the electrode due to the weak physical interaction, also observed, when BOD is electrostatically adsorbed on glassy carbon (GCE) modified by multi-walled CNTs (MWCNTs) (Al-Lolage et al., 2019).

Operational stability of the bioelectrode is another criterion for stability evaluation, which can usually be evaluated by chronoamperometry, chronopotentiometry etc. Here, we use the chronoamperometry technique to evaluate the current density of the BOD bioelectrode continuously in a time course of 60 h, applied with a potential of 0.2 V. Notably, the RGO-A bioelectrode shows superior operational stability with a half-lifetime of 55 h compared to RGO (13 h) and RGO-A_ads/BOD (40 h), Fig. 5b and S12b. The high RGO-A/BOD stability is assigned to the amide bonds between BOD lysine residues and the aromatic 4-ABA carboxylic groups on the graphene-based electrode surface, resulting in minimal leakage and activity loss of BOD (Gutiérrez-Sánchez et al., 2013). Exposed Lys21, Lys181 and Lys408 are proposed to be reactive towards 4-ABA carboxylic groups on the electrode (Singh et al., 2013). Especially, the operational stability of RGO-A bioelectrodes is the best as we can find in the literature for DET-type *Mv*BOD bioelectrodes under continuous operation (Table 1).

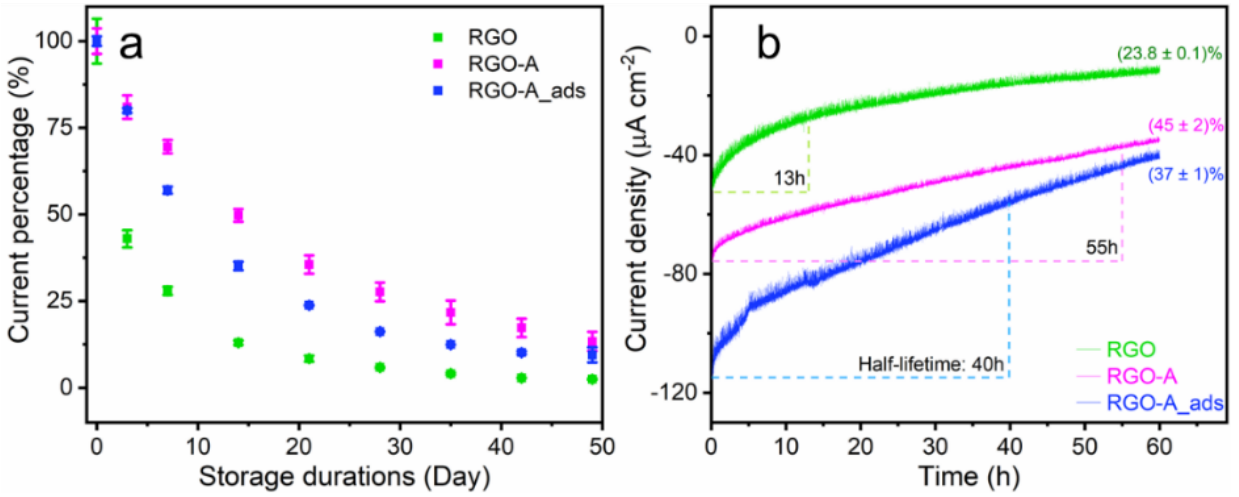

Fig. 5. (a) Storage and (b) operational lifetime of the BOD bioelectrodes on the matrices RGO and RGO-A via covalent bonding, and on RGO-A via physical adsorption (RGO-A_ads) in dioxygen-saturated and air-bubbled PBS (100 mM, pH 7.0). For storage lifetime evaluation, the catalytic activity was recorded by CV on a given day during the storage period. The operational stability of BOD bioelectrodes was evaluated by chronoamperometry with an applied potential of 0.2 V.

Table 1. Comparison of the operational stability of DET-type *Mv*BOD bioelectrodes at given applied potentials for ORR.

Matrix	Immobilization technique	Electrolyte	Operation half-lifetime	Operation conditions	Ref.
CPG/RGO-A	Covalent	PBS, pH 7.0	55 h	0.20 V, air purging	This work
CPG/RGO-A	Adsorption	PBS, pH 7.0	40 h	0.20 V, air purging	This work
Graphite/AuNPs-MPA	Covalent	Serum-mimic PBS, pH 7.4	~4 h	0.20 V, 500 rpm rotation	(Gutiérrez-Sánchez et al., 2013)
Au/MHA	Covalent	PBS, pH 6.0	~1 h (82%)*	0.20 V, air-saturated	(Gutierrez-Sanchez et al., 2016)
Buckypaper (MWCNTs)	Adsorption	PBS, pH 6.0	10 h	0.50 V, O_2-saturated, stirring	(Walgama et al., 2019)
GCE/MWCNTs-Cellulose	Adsorption	Citrate buffer, pH 5.0	45 h (60%)*	0.20 V, air purging	(Wu et al., 2009)
Au/CNTs/PANI	Adsorption	PBS, pH 7.4	12 h (78%)	0.045 V, air-saturated, stirring	(Parunova et al., 2016)

* Retention percentage of initial electrocatalytic activity. AuNPs: Au nanoparticles. MPA: mercaptopropionic acid. MHA: 6-mercaptohexanoic acid. CNTs: carbon nanotubes. PANI: Polyaniline. All potentials are vs. Ag/AgCl (sat.).

3.6 Applications as gas diffusion bioelectrodes and in EBFCs

RGO-A/BOD bioelectrodes have been finally exploited as a GDBE to demonstrate the versatile nature of our bioelectrode construction methodology (Higgins et al., 2011; So et al., 2017). GDBEs are gaining increasing attention as they accelerate the gaseous substrate supply (Chen et al., 2019;

Xia et al., 2016b), and possess great potential in portable and wearable EBFCs. GDBEs typically consist of a porous supporting electrode, a gas-diffusion layer, and a biocatalytic layer (So et al., 2017). The consumed gaseous substrate (O_2) for the ORR in the buffer solution can be steadily supplied from the gas phase. CPs are suitable as supporting electrodes. A GDBE cell specialized for membrane-less EBFCs was designed and fabricated (Fig. 6a, 6b, S13 and S14). RGO-A/BOD in an "air-breathing" configuration with gas phase filling of ambient air shows a higher Δj_{cat} of 60 µA cm^{-2} working at 0.2 V vs. Ag/AgCl, than the same electrode immersed in the electrolyte (40 µA cm^{-2}). The GDBE with enhanced dioxygen supply can thus significantly enhance the electrocatalytic performance, offering considerable potential for practical applications (So et al., 2014).

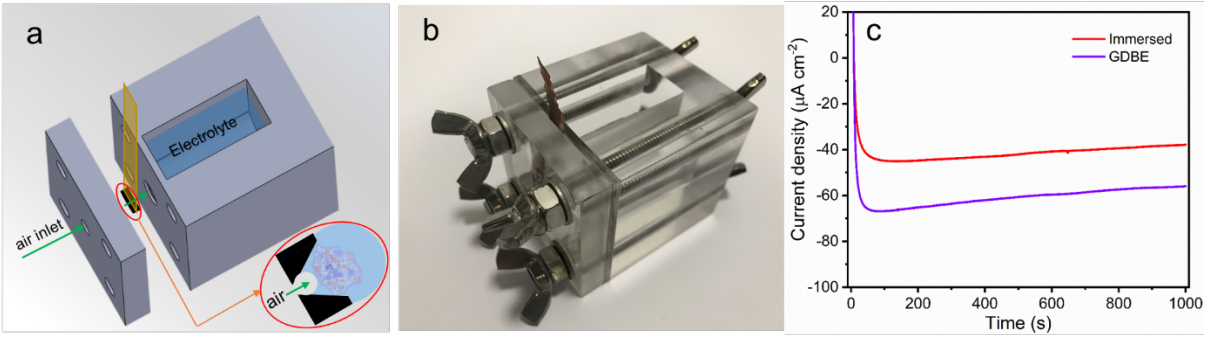

Fig. 6. (a) 3D view and (b) digital photo of the in-house built gas diffusion electrolyte cell. (c) Catalytic performance of the RGO-A/BOD bioelectrode as a GDBE electrode compared to the immersed bioelectrodes, evaluated by chronoamperometry with an applied potential of 0.2 V up to 1000 s.

The RGO-A/BOD in GDE configuration was finally assembled with a GOD/Os polymer based bioanode for EBFC applications to demonstrate the feasibility of the BOD biocathode and electricity generation from sugars. The bioanode undergoes mediated electron transfer between GOD and electrode, catalyzing two-electron oxidation of glucose. The constructed glucose/O_2 EBFCs delivered a maximum power density (P_{max}) of 22 µW cm^{-2} at 0.22 V, with a short current density of 193 µA cm^{-2} and an open circuit voltage (OCV) of 0.51 V (Fig. 7a), which is comparable to other graphene-based glucose/O_2 EBFCs (Shen et al., 2019a; Tang et al., 2020). The relatively

low power density of our constructed glucose/O_2 EBFC is due to the limitation by the non-optimized Os polymer/glucose oxidase bioanode, rather than the biocathode. EBFC applications of our RGO-A bioelectrode has in fact demonstrated the feasibility of the BOD biocathode and electricity generation from sugars.

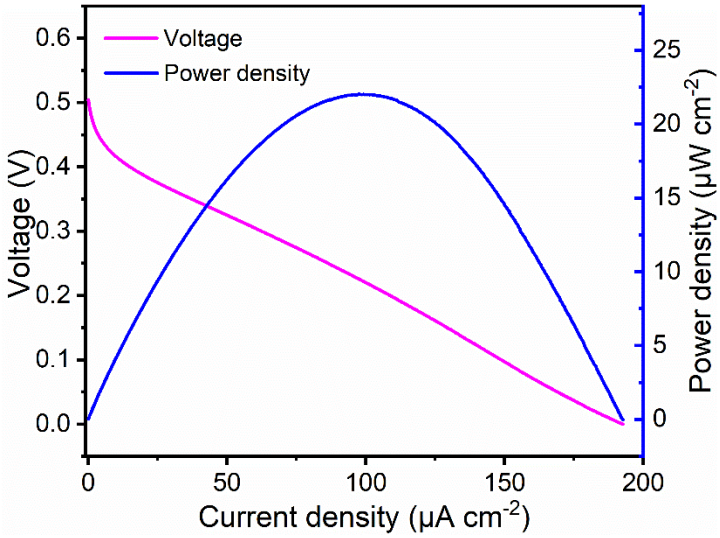

Fig. 7. Polarization and power density curves obtained from the GOD bioanode and BOD biocathode in air-equilibrated PBS (100 mM, pH 7.0) containing 20 mM glucose.

Conclusions

Controlled orientation of electron transfer proteins and redox enzymes on electrochemical surfaces for optimized facile interfacial electrochemical electron transfer is a recurrent challenge. We found that 4-ABA grafting alleviates reduced graphene oxide (RGO) aggregation, a core issue for electrochemical applications of RGO based materials. This new approach represents a universal strategy to retain the high electrochemical surface area and 3D structure of modified carbon paper electrodes, favorable for bioelectrochemical applications. The study offers novel outcomes and perspectives summarized here.

A unique and facile electrochemical pulse electrode treatment consisting of cathodic and anodic potential pulses alternatively has been introduced, with the cathodic pulse for graphene oxide

543 reduction and the anodic pulse for 4-ABA grafting. Our single-step electrochemical approach
544 combines in a novel facile synthesis carbon-based surface electrochemistry with robust chemical
545 surface immobilization of 4-ABA. The pulse waveform applied to the electrode has emerged as a
546 facile and promising means of achieving surface modification, in terms of convenience (time and
547 expensive electrochemical equipment) and controllability. However, upscaling of the process
548 might be a challenge by the nonuniform potential distribution of the quite large working electrode.
549 We have furthermore employed a wide range of techniques to map how 4-ABA grafting affects
550 the morphology, thickness and electrochemical properties of modified RGO-based electrodes.
551 Such investigations are rare but the core in the understanding of the interaction between the target
552 enzyme BOD and nanomaterials. Our work offers an intense characterization of modified RGO
553 sheets as supports for the enzyme BOD. This characterization has disclosed an in-depth
554 understanding on how modified nanomaterials enhance the productive interaction between the
555 target enzyme and the nanomaterial-modified electrode, as reflected clearly in the resulting
556 electrochemical performance of the new bioelectrode.

557 The bioelectrocatalytic performance of the bioelectrodes toward dioxygen reduction with the core
558 RGO-A/BOD surface was found to be the most efficient (the highest Δj_{cat} = 193 ± 4 μA cm^{-2})
559 among the bioelectrodes prepared and tested. The far superior DET-type biocatalytic performance
560 on the RGO-A matrix over that of the RGO matrix was identified to be caused mainly by more
561 favorable BOD orientation directed by the covalently linked 4-ABA aromatic groups on the
562 electrode surface. This could be supported by the numerical LSV analysis as a useful guide, based
563 on a crude distribution model (Léger et al., 2002; Xia et al., 2016a). Control experiments showed
564 that both negative and positive potential pulses in the surface modification process improve
565 significantly the orientation distribution as represented by the smallest core value of the parameter,
566 $\beta\Delta d$, compared to both the control surfaces and to other reported related carbon based surface types

(Takahashi et al., 2019; Xia et al., 2016a). Completive catalytic currents are thus obtained for RGO-A/BOD electrodes as for reported *Mv*BOD electrodes, but with much smaller amounts of drop-cast enzymes (Di Bari et al., 2016).

As a final major observation of our study, a merit of the new RGO-A/BOD bioelectrode is the operational stability. With a half-lifetime stability of 55 h the RGO-A/BOD bioelectrode stability also exceeds the stability of all previously reported *Mv*BOD electrode systems. This would be a particular merit in practical use such as in EBFCs. The high rate of interfacial electron transfer between BOD and the 3D matrix and the high stability of the RGO-A/BOD bioelectrode are likely ascribed to alleviation of the RGO aggregation due to the electrostatic repulsion among the 4-ABA-functionalized RGO sheets and a retention of a high surface area. The dual roles of grafting of 4-ABA, at the same time as a bioelectrochemical electron transfer promotor and as an efficient enzyme stabilizer are thus highlighted by the results of our study.

In summary, the alleviation of RGO aggregation is important and the methodologies, especially the grafting of functional groups for alleviated RGO aggregation, and the strong stabilization of the integrated functional RGO-A/BOD unit proposed in this work can most likely be extended to other electrochemical RGO and carbon-based applications, in this way opening new entrance for pure and applied bioelectrochemistry.

Declaration of competing interest

There are no conflicts to declare.

Acknowledgements

Financial support from The Danish Council for Independent Research for the YDUN project (DFF 4093-00297) and the Carlsberg foundation (2012_01_0520) is gratefully acknowledged. This

591 project has received funding from the European Union's Horizon 2020 research and innovation
592 program under the Marie Skłodowska-Curie grant agreement No. 713683. X.Y. and W.H.
593 acknowledge support from the China Scholarship Council (CSC, 201806650009 and
594 201706220080). J.U. acknowledges support from the Russian Science Foundation (Project Nos.
595 17-13-01274 and 17-03-00619a). Dr. Hong-qi Xia is acknowledged for the kind discussion. Prof.
596 Dónal Leech is acknowledged for kindly delivering the Os complex modified polymer.

597 Appendix A. Supplementary data

598 Supplementary data to this article can be found online at xxx.

599 References

600 Al-Lolage, F.A., Bartlett, P.N., Gounel, S., Staigre, P., Mano, N., 2019. ACS Catal. 9(3), 2068-2078.
601 Barbier, B., Pinson, J., Desarmot, G., Sanchez, M., 1990. J. Electrochem. Soc. 137(6), 1757-1764.
602 Blanford, C.F., Foster, C.E., Heath, R.S., Armstrong, F.A., 2009. Faraday Discussions 140(0), 319-335.
603 Chen, X., Yin, L., Lv, J., Gross, A.J., Le, M., Gutierrez, N.G., Li, Y., Jeerapan, I., Giroud, F., Berezovska, A.,
604 O'Reilly, R.K., Xu, S., Cosnier, S., Wang, J., 2019. Adv. Funct. Mater. 29(46), 1905785.
605 Chi, Q., Farver, O., Ulstrup, J., 2005. PANS 102(45), 16203-16208.
606 Christenson, A., Shleev, S., Mano, N., Heller, A., Gorton, L., 2006. BBA-Bioenergetics 1757(12), 1634-1641.
607 Cracknell, J.A., McNamara, T.P., Lowe, E.D., Blanford, C.F., 2011. Dalton Trans. 40(25), 6668-6675.
608 Di Bari, C., Goñi-Urtiaga, A., Pita, M., Shleev, S., Toscano, M.D., Sainz, R., De Lacey, A.L., 2016. Electrochim.
609 Acta 191, 500-509.
610 Dreyer, D.R., Park, S., Bielawski, C.W., Ruoff, R.S., 2010. Chem. Soc. Rev. 39(1), 228-240.
611 Durand, F., Kjaergaard, C.H., Suraniti, E., Gounel, S., Hadt, R.G., Solomon, E.I., Mano, N., 2012. Biosens.
612 Bioelectron. 35(1), 140-146.
613 Gray, H.B., Winkler, J.R., 2010. BBA-Bioenergetics 1797(9), 1563-1572.
614 Gross, A.J., Chen, X., Giroud, F., Travelet, C., Borsali, R., Cosnier, S., 2017. J. Am. Chem. Soc. 139(45), 16076-
615 16079.
616 Gutierrez-Sanchez, C., Ciaccafava, A., Blanchard, P.Y., Monsalve, K., Giudici-Orticoni, M.T., Lecomte, S.,
617 Lojou, E., 2016. ACS Catal. 6(8), 5482-5492.
618 Gutiérrez-Sánchez, C., Pita, M., Toscano, M.D., De Lacey, A.L., 2013. Electroanalysis 25(6), 1359-1362.
619 Hernández-Cancel, G., Suazo-Dávila, D., Ojeda-Cruzado, A.J., García-Torres, D., Cabrera, C.R., Griebenow,
620 K., 2015. J. Nanobiotechnol. 13(1), 70.
621 Higgins, S.R., Lau, C., Atanassov, P., Minteer, S.D., Cooney, M.J., 2011. ACS Catal. 1(9), 994-997.
622 Korani, A., Salimi, A., 2015. Electrochim. Acta 185, 90-100.
623 Lalaoui, N., Le Goff, A., Holzinger, M., Cosnier, S., 2015. Chem. Eur. J. 21(47), 16868-16873.
624 Lawal, A.T., 2019. Biosens. Bioelectron. 141, 111384.

Le, T.X.H., Bechelany, M., Engel, A.B., Cretin, M., Tingry, S., 2016. Electrochim. Acta 219, 121-129.
Léger, C., Jones, A.K., Albracht, S.P.J., Armstrong, F.A., 2002. J. Phys. Chem. B 106(50), 13058-13063.
Li, X., Li, D., Zhang, Y., Lv, P., Feng, Q., Wei, Q., 2020. Nano Energy 68, 104308.
Li, X., Xu, Y., Hu, G., Luo, Z., Xu, D., Tang, T., Wen, J., Li, M., Zhou, T., Cheng, Y., 2018. Electrochim. Acta 280, 33-40.
Lopez, R.J., Babanova, S., Ulyanova, Y., Singhal, S., Atanassov, P., 2014. ChemElectroChem 1(1), 241-248.
Mano, N., de Poulpiquet, A., 2018. Chem. Rev. 118(5), 2392-2468.
Mazurenko, I., Monsalve, K., Rouhana, J., Parent, P., Laffon, C., Goff, A.L., Szunerits, S., Boukherroub, R., Giudici-Orticoni, M.-T., Mano, N., Lojou, E., 2016. ACS Appl. Mater. Inter. 8(35), 23074-23085.
Moser, C.C., Keske, J.M., Warncke, K., Farid, R.S., Dutton, P.L., 1992. Nature 355(6363), 796-802.
Murata, K., Kajiya, K., Nakamura, N., Ohno, H., 2009. Energy Environ. Sci. 2(12), 1280-1285.
Olejnik, P., Palys, B., Kowalczyk, A., Nowicka, A.M., 2012. J. Phys. Chem. C 116(49), 25911-25918.
Parunova, Y.M., Bushnev, S.O., Gonzalez-Arribas, E., Falkman, P., Lipkin, A.V., Popov, V.O., Shleev, S.V., Pankratov, D.V., 2016. Russian J. Electrochem. 52(12), 1166-1171.
Pavlidis, I.V., Patila, M., Bornscheuer, U.T., Gournis, D., Stamatis, H., 2014. Trends Biotechnol. 32(6), 312-320.
Poon, K.C., Ma, X., Tan, D.C.L., Su, H., Sato, H., 2018. ACS Catal. 8(6), 4950-4954.
Qiu, H.-J., Guan, Y., Luo, P., Wang, Y., 2017. Biosens. Bioelectron. 89, 85-95.
Ruff, A., Szczesny, J., Marković, N., Conzuelo, F., Zacarias, S., Pereira, I.A.C., Lubitz, W., Schuhmann, W., 2018. Nat. Commun. 9(1), 3675.
Samejima, T., Wu, C.-S.C., Shiboya, K., Kaji, H., Koikeda, S., Ando, K., Yang, J.T., 1994. J. Protein Chem. 13(3), 307-313.
Seselj, N., Engelbrekt, C., Ding, Y., Hjuler, H.A., Ulstrup, J., Zhang, J., 2018. Adv. Energy Mater. 8(13), 1702609.
Shen, F., Pankratov, D., Halder, A., Xiao, X., Toscano, M.D., Zhang, J., Ulstrup, J., Gorton, L., Chi, Q., 2019a. Nanoscale Adv. 1(7), 2562-2570.
Shen, F., Pankratov, D., Pankratova, G., Toscano, M.D., Zhang, J., Ulstrup, J., Chi, Q., Gorton, L., 2019b. Bioelectrochemistry 128, 94-99.
Siepenkoetter, T., Salaj-Kosla, U., Xiao, X., Belochapkine, S., Magner, E., 2016. Electroanalysis 28(10), 2415-2423.
Siepenkoetter, T., Salaj-Kosla, U., Xiao, X., Conghaile, P.Ó., Pita, M., Ludwig, R., Magner, E., 2017. ChemPlusChem 82(4), 553-560.
Singh, K., McArdle, T., Sullivan, P.R., Blanford, C.F., 2013. Energy Environ. Sci. 6(8), 2460-2464.
So, K., Kawai, S., Hamano, Y., Kitazumi, Y., Shirai, O., Hibi, M., Ogawa, J., Kano, K., 2014. Phys. Chem.Chem. Phys. 16(10), 4823-4829.
So, K., Sakai, K., Kano, K., 2017. Curr. Opin. Electrochem. 5(1), 173-182.
Takahashi, Y., Wanibuchi, M., Kitazumi, Y., Shirai, O., Kano, K., 2019. J. Electroanal. Chem. 843, 47-53.
Tang, J., Werchmeister, R.M.L., Preda, L., Huang, W., Zheng, Z., Leimkühler, S., Wollenberger, U., Xiao, X., Engelbrekt, C., Ulstrup, J., Zhang, J., 2019. ACS Catal. 9(7), 6543-6554.
Tang, J., Yan, X., Engelbrekt, C., Ulstrup, J., Magner, E., Xiao, X., Zhang, J., 2020. Bioelectrochemistry 134, 107537.
Trasatti, S., Petrii, O.A., 1991. Pure Appl. Chem. 63(5), 711.
Walgama, C., Pathiranage, A., Akinwale, M., Montealegre, R., Niroula, J., Echeverria, E., McIlroy, D.N., Harriman, T.A., Lucca, D.A., Krishnan, S., 2019. ACS Appl. Bio. Mater. 2(5), 2229-2236.

669 Wang, F.-T., Wang, Y.-H., Xu, J., Huang, K.-J., Liu, Z.-h., Lu, Y.-f., Wang, S.-y., Han, Z.-w., 2020. Nano Energy
670 68, 104310.
671 Wei, S., Hao, Y., Ying, Z., Xu, C., Wei, Q., Xue, S., Cheng, H.-M., Ren, W., Ma, L.-P., Zeng, Y., 2020. J. Mater.Sci.
672 Technol. 37, 71-76.
673 Werchmeister, R.M.L., Tang, J., Xiao, X., Wollenberger, U., Hjuler, H.A., Ulstrup, J., Zhang, J., 2019. J.
674 Electrochem. Soc. 166(16), G170-G177.
675 Wernert, V., Lebouin, C., Benoit, V., Gadiou, R., de Poulpiquet, A., Lojou, E., Denoyel, R., 2018. Electrochim.
676 Acta 283, 88-96.
677 Wu, X., Zhao, F., Varcoe, J.R., Thumser, A.E., Avignone-Rossa, C., Slade, R.C.T., 2009. Biosens. Bioelectron.
678 25(2), 326-331.
679 Xia, H.-q., Kitazumi, Y., Shirai, O., Kano, K., 2016a. J. Electroanal. Chem. 763, 104-109.
680 Xia, H.-q., So, K., Kitazumi, Y., Shirai, O., Nishikawa, K., Higuchi, Y., Kano, K., 2016b. J. Power Sources 335,
681 105-112.
682 Xiao, X., Conghaile, P.Ó., Leech, D., Ludwig, R., Magner, E., 2017. Biosens. Bioelectron. 90, 96-102.
683 Xiao, X., McGourty, K.D., Magner, E., 2020. J. Am. Chem. Soc. 142(26), 11602-11609.
684 Xiao, X., Siepenkoetter, T., Conghaile, P.Ó., Leech, D., Magner, E., 2018. ACS Appl. Mater. Inter. 10(8),
685 7107-7116.
686 Xiao, X., Xia, H.-q., Wu, R., Bai, L., Yan, L., Magner, E., Cosnier, S., Lojou, E., Zhu, Z., Liu, A., 2019. Chem.
687 Rev. 119, 9509-9558.
688 Yang, G., Shen, Y., Wang, M., Chen, H., Liu, B., Dong, S., 2006. Talanta 68(3), 741-747.
689 Yang, K., Chen, B., Zhu, L., 2015. Sci. Rep. 5(1), 11641.
690 Yu, Y., Nyein, H.Y.Y., Gao, W., Javey, A., 2019. Adv. Mater., 1902083.
691 Zhao, C.-e., Gai, P., Song, R., Chen, Y., Zhang, J., Zhu, J.-J., 2017. Chem. Soc. Rev. 46(5), 1545-1564.
692 Zhao, G., Jiang, L., He, Y., Li, J., Dong, H., Wang, X., Hu, W., 2011. Adv. Mater. 23(34), 3959-3963.
693
694

695 **Graphic TOC**:

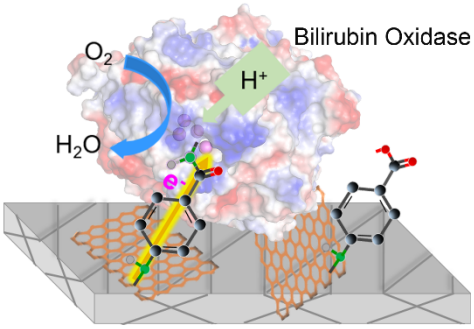

696
697